NANOROBOTICS

A self-assembled nanoscale robotic arm controlled by electric fields

Enzo Kopperger,[1]* Jonathan List,[1]* Sushi Madhira,[2] Florian Rothfischer,[1]
Don C. Lamb,[2,3,4] Friedrich C. Simmel[1,4]†

The use of dynamic, self-assembled DNA nanostructures in the context of nanorobotics requires fast and reliable actuation mechanisms. We therefore created a 55-nanometer–by–55-nanometer DNA-based molecular platform with an integrated robotic arm of length 25 nanometers, which can be extended to more than 400 nanometers and actuated with externally applied electrical fields. Precise, computer-controlled switching of the arm between arbitrary positions on the platform can be achieved within milliseconds, as demonstrated with single-pair Förster resonance energy transfer experiments and fluorescence microscopy. The arm can be used for electrically driven transport of molecules or nanoparticles over tens of nanometers, which is useful for the control of photonic and plasmonic processes. Application of piconewton forces by the robot arm is demonstrated in force-induced DNA duplex melting experiments.

N anoscale robotic systems will enable the programmable synthesis and assembly of molecular materials from the bottom up. Components of such systems were previously created with the tools of supramolecular chemistry (1–4) and bionanotechnology (5). In particular, DNA self-assembly (6, 7) has been used successfully to create nanoscale robotic walkers (8–13), assembly lines (14), movable molecular arms (15–18), and molecular mechanisms (19, 20). However, as a result of being driven by DNA hybridization reactions (8–10, 13–16, 18, 19), deoxyribozyme (11) or enzyme (12) action, changes in buffer composition, or using photoswitchable components (17), these systems were very slow, had a low assembly or operation yield, or were unable to exert appreciable forces against external loading. In one of the most successful methodologies (21, 22), DNA machines are driven through their operation cycle by hybridization with fuel and antifuel strands using toehold-mediated strand displacement reactions. Although this approach has the advantage of sequence addressability, DNA hybridization and strand-exchange reactions are slow, and structural switching often occurs with low yield. In our experiment, we deliberately abandoned sequence-specific switching and used electrical fields to move the components of a DNA machine with respect to each other. We thus gain many orders of magnitude in operation speed, almost perfect switching yield, and the capability of computer-controlled nanoscale motion and positioning.

A DNA-based molecular platform with an integrated robotic arm

The actuator unit of our system is composed of a 55-nm–by–55-nm DNA origami plate with an integrated 25-nm-long arm defined by a DNA six-helix bundle (6HB) (Fig. 1A), allowing for a high-yield, one-pot folding procedure. For the rigid DNA plate, we used a crossed two-layer scaffold routing in which the top layer is rotated by 90° with respect to the bottom layer (supplementary materials and methods) (23). The 6HB,

functioning as the robot arm, is connected to the top layer of the base plate via a flexible joint created by two adjacent scaffold crossovers with three and four unpaired bases, respectively (see supplementary text section on the design of the joint) (23). Successful assembly of the structure with ≈90% yield was verified using transmission electron microscopy (TEM) and atomic force microscopy (AFM) (Fig. 1, B and C, and fig. S1) (23). Consistent with our design, AFM indicates a height of 4 nm for the base plate and an additional 4 nm for the 6HB arm.

We first used single-molecule multicolor Förster resonance energy transfer (FRET) experiments to investigate diffusive motion of the arm with respect to the base plate (Fig. 2). For these experiments, we extended two staple strands on opposite sides of the plate with an identical short docking sequence, whereas a staple strand on the arm was extended with the complementary sequence. Transient binding of the arm results in stochastic switching between the two docking sites, which we observed with the help of three reporter dyes: a FRET donor at the tip of the arm and two different acceptor dyes at the docking sites (Fig. 2A). A typical trace of stochastically alternating FRET signals is shown in Fig. 2B. Upon donor excitation, a high donor fluorescence (blue) indicates a freely diffusing arm, whereas a high acceptor fluorescence (green or red) indicates docking at the respective site. Dwell times for the three states were extracted from fluorescence traces of more than 1000 robot-arm platforms via a hidden Markov model analysis (24) (fig. S2 and supplementary methods) (23). As expected, the dwell time in the bound states increases with docking duplex length (Fig. 2C, top). The dwell time spent in the unbound state also increases (Fig. 2C, bottom), indicating slower diffusion and/or a reduced hybridization rate for

Fig. 1. A molecular platform with an integrated rotatable positioning arm. (**A**) Sketch of the DNA origami structure in side (top left) and top (right) view. The close-up in the perspective view (bottom left) highlights the single-stranded scaffold crossovers that form the flexible joint. (**B**) TEM class-average (top) and single-particle (bottom) micrographs of the structure. (**C**) AFM image of particles on mica. Only structures for which the actuator arms are buried below the plates could be imaged with high contrast. For imaging, the arms were fixed to the plates with a 10-bp duplex formed between two staple extensions on the plate and the tip of the arm. (Inset) Height profile of a platform measured along the direction indicated by the red arrow.
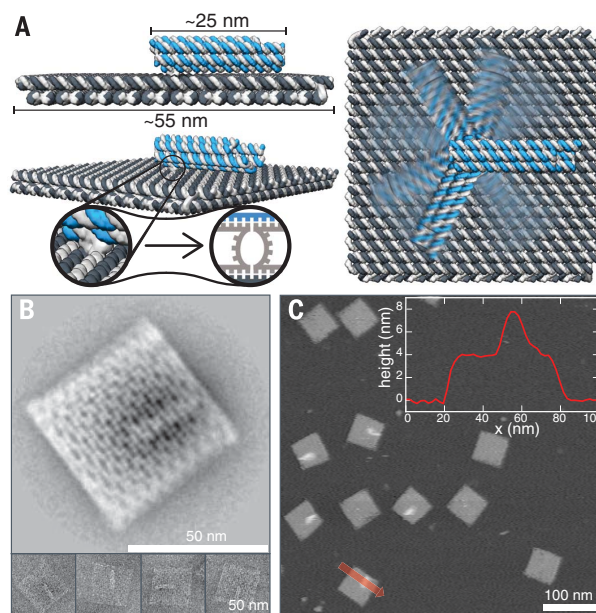
[1]Physics Department E14, Technical University Munich, 85748 Garching, Germany. [2]Department of Chemistry, Ludwig-Maximilians University Munich, 81377 Munich, Germany. [3]Center for Integrated Protein Science Munich, Ludwig-Maximilians University Munich, 81377 Munich, Germany. [4]Nanosystems Initiative Munich, 80539 Munich, Germany.
*These authors contributed equally to this work.
†Corresponding author. Email: simmel@tum.de
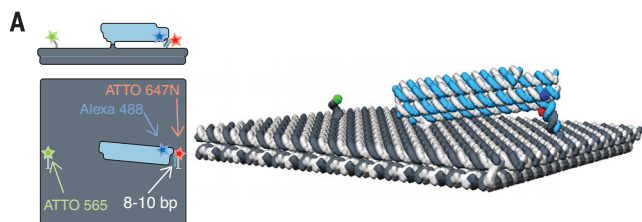
Fig. 2. Stochastic switching experiments. (**A**) For single-molecule multicolor FRET experiments, a donor fluorophore (Alexa Fluor 488) is attached to the six-helix bundle (6HB) arm and two acceptor fluorophores (ATTO 565 and ATTO 647N) are connected to staple-strand extensions on opposite sides of the plate. The pictograms on the left show hybridization of an extended staple of the arm to the staple extension of the base plate labeled with ATTO 647N. The length of the docking duplex was varied between 8 and 10 bp. A schematic three-dimensional representation is shown on the right. (**B**) Fluorescence traces obtained from the three fluorophores during donor excitation of the structures containing 9-bp docking duplexes. The change between green and red fluorescence indicates switching of the arm between corresponding docking sites. The zoomed-in view (bottom) reveals short periods of free diffusion between unbinding and rebinding events during which the donor (blue) fluorescence is dominant. a.u., arbitrary units. (**C**) Average dwell times for the bound and unbound states and their dependence on duplex length. Dwell times for the bound states (high acceptor signals shown in red or green; top panel) correspond to the times spent at the respective docking site. Dwell times for the unbound state (high donor signal shown in blue; bottom panel) represent the length of the traversal periods of the freely diffusing arm. (**D**) Average durations of the unbound states for various transitions and their dependence on duplex length. Corresponding to the start and end points of the traversal period (docking site or bound state shown in green or red before and after the unbound state), the unbound states can be classified as green→red and green→green or red→green and red→red traversals. In (C) and (D), the error bars denote the SD of the mean from three independent measurements.
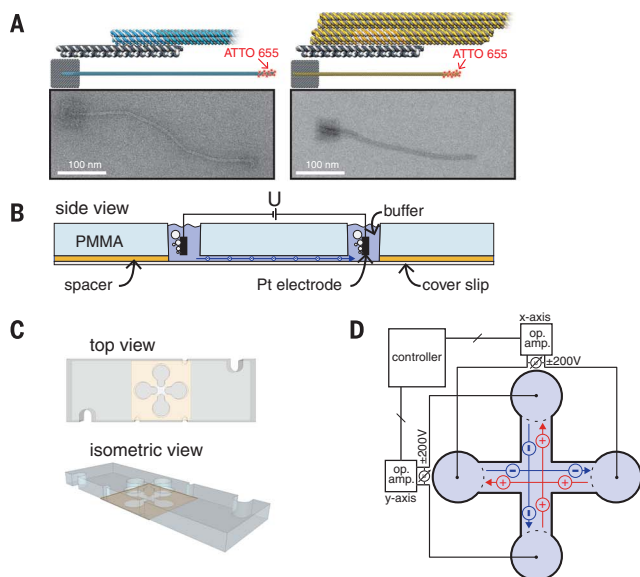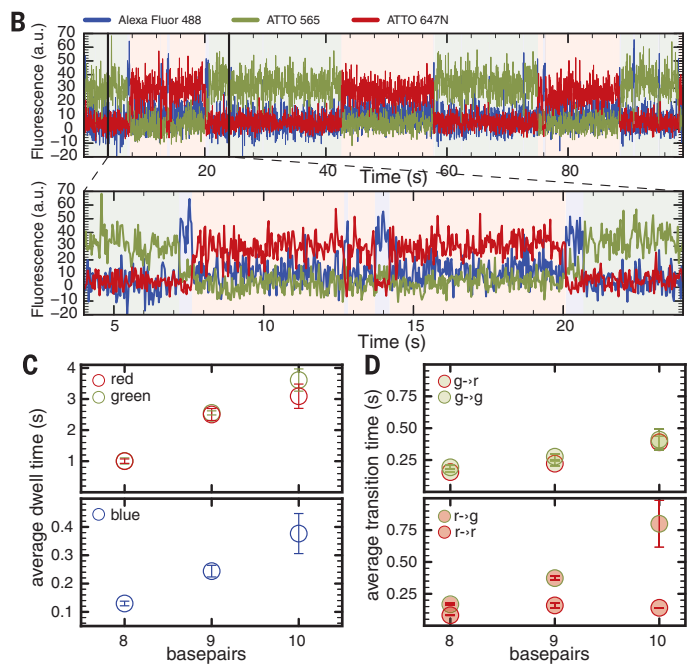
Fig. 3. External electric control of the robotic arm. (**A**) Two pointer extension designs for the robot arm and corresponding TEM images. The blue, linear extension pointer has a length of 411 nm (total length from center of rotation to tip: 436 nm). The orange pointer has a shape-complementary connection that withstands higher torque (total length: 354 nm; pivot point to tip: 332 nm; resulting arm extension: 308 nm). (**B**) Cross section and (**C**) top and isometric view of the cross-shaped electrophoretic sample chamber. PMMA, poly(methyl methacrylate); U, voltage. (**D**) Schematic depiction of the experimental setup with four electrodes. (**E**) Fluorescence microscopy images of three structures that are switched in the electric field. For the highlighted particle, movements are shown as snapshots and kymographs. The green and blue arrows indicate
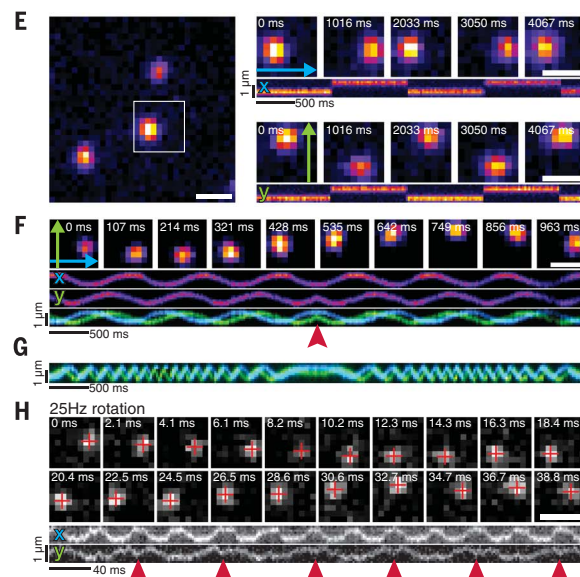
the axes chosen for the kymographs. (Top) Switching left and right with 1 Hz. (Bottom) Switching up and down with 1 Hz. (**F**) (Top) One clockwise turn of 1-Hz rotation. (Bottom) Kymographs showing multiple turns of clockwise rotation followed by multiple counterclockwise turns, separately for the x and y axes and as a blue and green overlay. Reversal of the voltage and, thus, of the rotation direction is indicated by the red arrowhead (movie S1) (23). (**G**) Kymographs (x and y projections) obtained from a frequency sweep from 0 to 8 Hz and back, shown as an overlay of the kymographs along the x and y axes. (**H**) High-speed 360° clockwise and counter-clockwise rotation with 25 Hz. For each frame, the center of the pointer tip is indicated by a red cross. Reversal of the rotation direction is indicated by red arrowheads (movie S2) (23). Unlabeled scale bars, 1 μm.
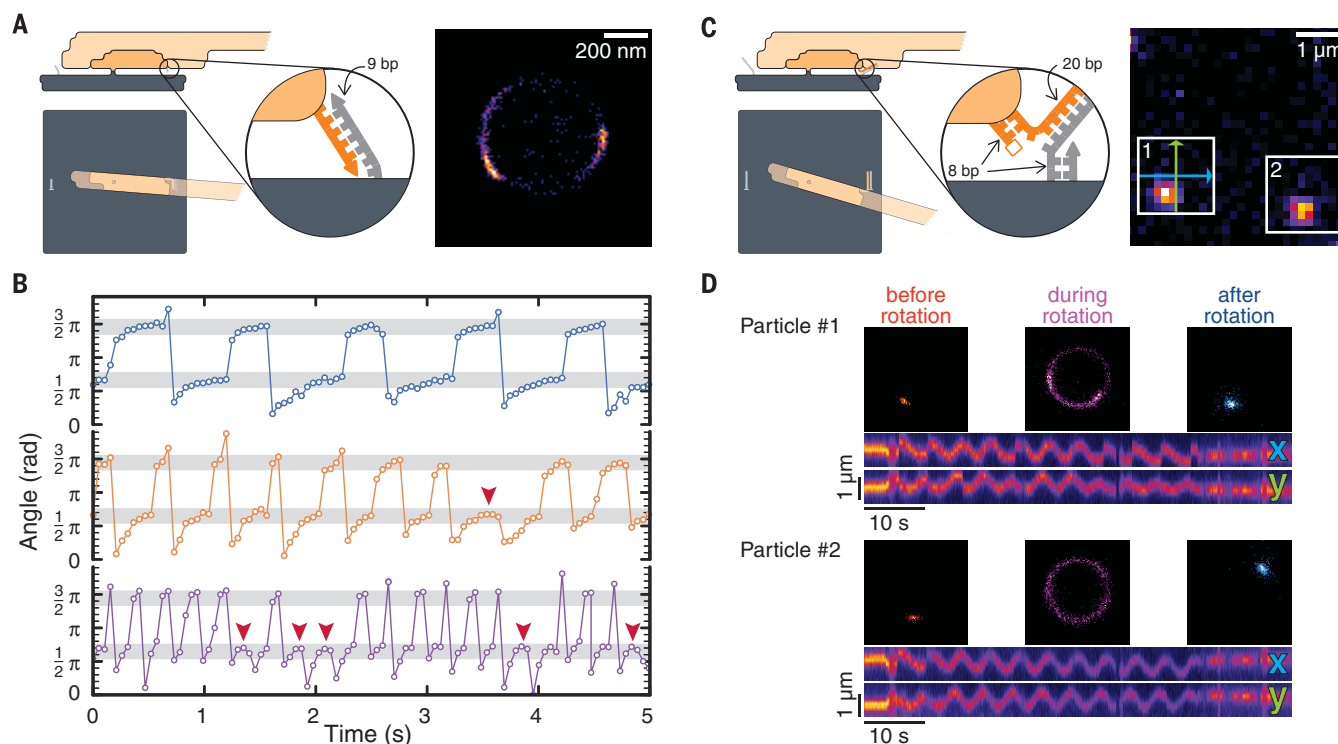
Fig. 4. Controlled hybridization and force-induced duplex dissociation.
(**A**) Field-controlled switching of the extended robot arm between two 9-bp docking positions. (Left) Scheme of the setup. (Right) Single-molecule localization image of pointer positions acquired during electrical rotation at 1 Hz. The number of localizations is increased at angles corresponding to the two docking positions. (**B**) Angle plotted over time for 1-, 2-, and 4-Hz rotation with 110 V. The arm shows pronounced lagging for two angles (highlighted by gray bands). Higher frequencies result in a larger number of missed turns, which are indicated by the red arrowheads. (**C**) Unzipping of a 20-bp DNA duplex with the extended robot arm. (Left) Extensions from the platform and from the arm feature a short 8-bp strain-relief domain that prevents the staple strands from being pulled out of the structure. (Right) Experiments with two example particles are shown. Without an electric field, the arm is fixed at one of two docking positions on the base plate. (**D**) Rotation requires unzipping of the duplex, which is shown in the images (red, before rotation; violet, during rotation; and blue, after rotation) and kymographs at the bottom. Particle #1 rebinds to the starting position, whereas particle #2 rebinds to the position on the opposite side.

longer docking duplexes. Observed state transitions can be classified into transitions from one binding site to the other (green→red or red→green) or rebinding events to the same docking site (green→green or red→red). When the arm initially unbinds from the green docking site, it binds to either site with roughly the same transition time (Fig. 2D, top). Conversely, arms starting at the red docking site have a higher tendency to return to the same site (Fig. 2D, bottom). This bias is consistent with the expected orientation of the arm on the base plate, which is designed to point toward the red docking site (see Fig. 1A). The corresponding higher effective concentration of the arm in the vicinity of the red docking site results in faster rebinding transitions (16). Photophysical origins of the observed changes in the FRET signal (such as fluorescent dark states or environmental quenching of the fluorophores) were excluded by performing millisecond alternating laser excitation (25) experiments (fig. S3 and supplementary materials and methods) (23).

## Modular extension with pointer structures

To facilitate direct observation of the arm's motion by diffraction-limited fluorescence microscopy,

we designed two versions of pointer structures that were multiply labeled with the fluorophore ATTO 655. Version one extended the arm linearly by 411 nm (Fig. 3A, blue). Version two extended the arm by 308 nm (Fig. 3A, orange) and was modularly plugged into the robot arm via a shape-complementary connector structure, creating a more stable connection between pointer and arm to allow for better torque transmission. Both pointers are based on a rigid 6HB with a persistence length >1 μm (26). The two designs were motivated by the differing requirements for the experiments described below. For rotational diffusion experiments in the absence of docking sites, we found that the linear pointer interacted less with the base plate than the shape-complementary pointer (fig. S4) (23). However, when used to exert forces, the linear pointer displayed a reduced stability and tended to break at the connection site (supplementary text) (23). In the presence of docking sites, single-molecule localization images of both pointers were consistent with the positions of the docks on the platform, proving that the extensions point along the axis of the short arm (fig. S5) (23) and that the interactions with the docking sites dominated over unspecific sticking.

Electrical control of the robot arm

To realize dynamic external control of the robot arm, we applied electrical fields to the system—a natural choice for the manipulation of charged biomolecules (27). Electrical fields have been previously used only to stretch or orient substrate-immobilized DNA duplexes (28) but not to dynamically control the conformation of nanomechanical DNA devices. We created a cross-shaped electrophoretic chamber constituted by two perpendicular fluidic channels intersecting at the center of a microscopy cover slip, with two pairs of platinum electrodes inserted into the four buffer reservoirs (Fig. 3, B and C, and fig. S6) (23). DNA nanostructures immobilized at the center of the cross chamber experience a superposition of the fields generated by the electrode pairs. Hence, a voltage can be applied to arbitrarily control the pointing direction of the arm (Fig. 3D).

Electrical actuation of the arms results in a movement of the pointers, which we observed with an electron-multiplying charge-coupled device camera using total internal reflection fluorescence (TIRF) microscopy. In Fig. 3, we show switching of an arm in two perpendicular directions (Fig. 3E), as well as rotation with a constant frequency of 1 Hz (Fig. 3F) and with variable
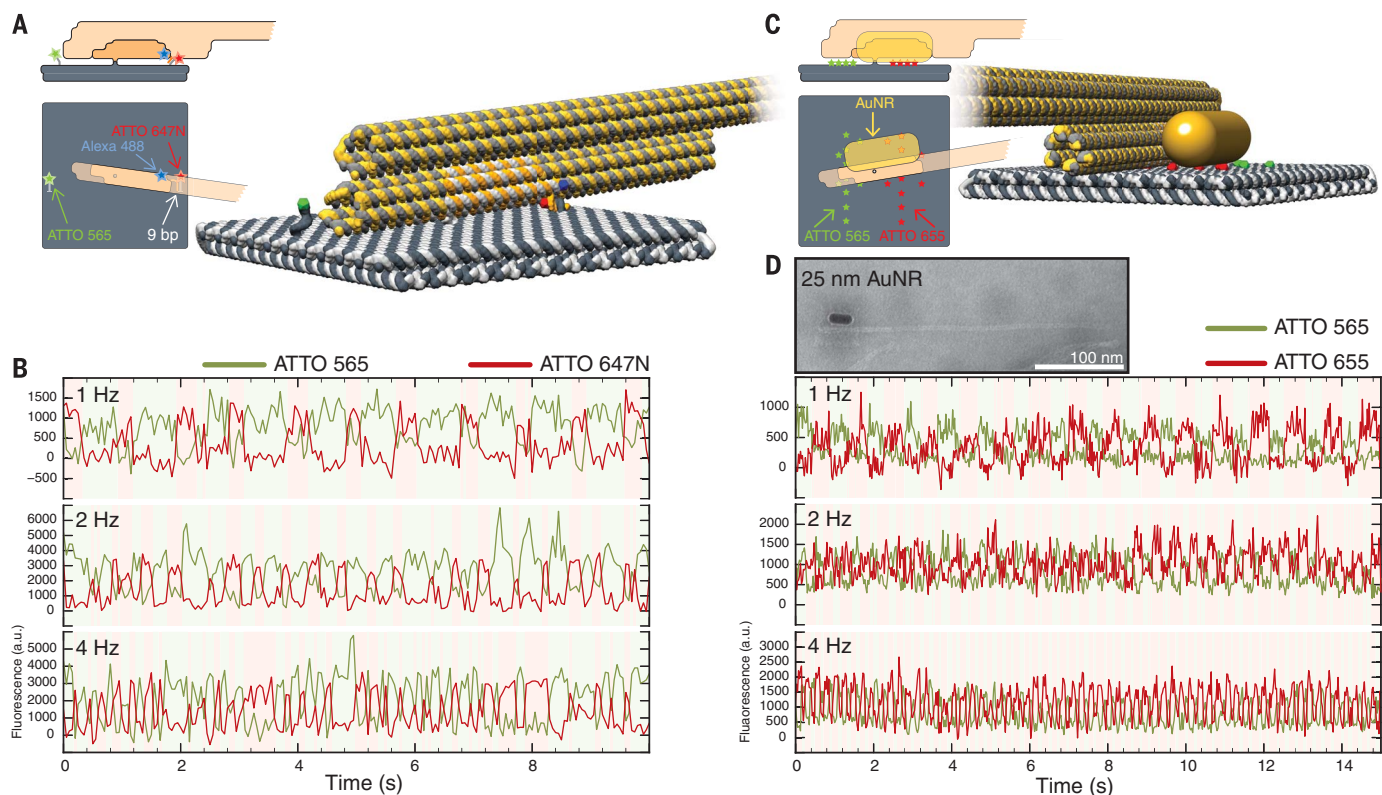
Fig. 5. Electrically controlled movement of molecules and nanoparticles. (**A**) Configuration of the robot arm with shape-complementary extension for transport of the FRET donor Alexa Fluor 488 between two 9-nucleotide docking sites with the acceptors ATTO 565 and ATTO 647N. (**B**) Acceptor signals for continuous donor excitation for electrical rotation at 1 Hz (top), 2 Hz (middle), and 4 Hz (bottom). (**C**) For application of the robot arm in switchable plasmonics, a 25-nm-long gold nanorod (AuNR) is attached to the side of the 6HB arm, and 11 ATTO 565 and ATTO 655 dyes are placed on opposite halves of the platform. (**D**) (Top) TEM micrograph of a structure with a 25-nm AuNR. (Bottom) Fluorescence traces for continuous excitation of the dyes while the robot arm is rotated at 1, 2, and 4 Hz (fig. S12) (*23*) for data obtained with a 50-nm AuNR.

frequency (Fig. 3G), ramping from 0 to 8 Hz and back to 0 Hz. Movie S1 (*23*) shows a range of movement patterns, underlining the capability of arbitrary angular control. To characterize faster arm movements, we used a complementary metal-oxide semiconductor camera to record TIRF microscopy videos with a 2-ms time resolution. An image series taken from a video in which the robot arm was rotated back and forth at a frequency f = 25 Hz is shown in Fig. 3H (see also supplementary movie S2) (*23*). Kymographs displaying the projected motion of the arm's pointer along the x and y axes show the expected sinusoidal characteristics. In a high-viscosity buffer solution containing 65% sucrose, motion of the arm was substantially slowed (fig. S7) (*23*).

Next, we assessed the angular positioning precision of the arm, which can be achieved in the absence of docking sites by the electrical field alone (fig. S8) (*23*). For large applied voltages (≥120 V in our setup), the angular standard deviation is ≈0.1 radians, which translates to a positioning precision of ≈2.5 nm on the plate.

Controlled interaction with docking positions on the platform

To investigate the interaction of the arm with binding sites on the platform during electrical manipulation, we performed latching experiments with the same arrangement of docks as in Fig. 2 and an identical 9–base pair (bp) docking sequence (Fig. 4A). When rotated at frequencies of f = 1, 2, and 4 Hz, we observed temporary stalling of the pointer at the two angle positions that correspond to the two docking sites (Fig. 4B), indicating that the arm snaps into the binding positions during rotation. Whereas the signal followed the external control faithfully for f = 1 Hz, occasional skips occurred for f = 2 and 4 Hz. This behavior is caused by the statistical nature of single-molecule duplex dissociation, whose frequency increases exponentially with the application of a force (*29*) and, in dynamic experiments, also depends on the force rate (*29*). Apparently, the dissociation rate (~0.4 s^{-1}) (Fig. 2B) of the docking duplex is sufficiently enhanced by the electrical force to follow the 1-Hz rotation. For higher frequencies, the duplex does not always dissociate fast enough and the arm cannot follow the rotation of the electrical field. By contrast, at a slower rotation speed of f = 0.1 Hz, we were able to observe dynamic latching to four different docking sites (fig. S9) (*23*).

We next tested whether the robotic arm could wrest apart a 20-bp docking duplex, which is a stable structure at room temperature. Although the arm is firmly locked in place in the absence of an electrical field, it can be released from the docking site by actuating the arm and rotated as shown in Fig. 4, C and D. Unzipping is expected to be most effective when the field is applied perpendicularly to the fixed arm. As the base plates are randomly oriented with respect to the sample chamber, the field is slowly rotated at a frequency of 0.2 Hz to guarantee that each structure has sufficient time to experience a strong enough unzipping force. When switching off the field during rotation at an arbitrary phase, the arm immediately localizes to an available docking site.

At the field strengths generated in our sample chamber, we do not expect field-induced melting of DNA duplexes as is observed, for instance, for DNA structures immobilized on electrode surfaces (*30*). Instead, the arm acts as a lever that mechanically transduces the electrical force acting on its large charge to the docking duplex. Force-induced unzipping of DNA duplexes has been previously achieved through the use of single-molecule manipulation techniques such as AFM (*31*) and optical tweezers (*32*) or within nanopores (*33*). These experiments have shown that DNA unzipping requires forces on the order of 10 to 20 pN, consistent with the typical binding free energy of DNA base pairs and their subnanometer spacing. A rough theoretical treatment (supplementary text) (*23*) suggests that forces that can be

generated by the robot arm are on this scale. The ability to separate stable duplexes by force facilitates the electrically controlled dissociation of the arm from one docking site and its subsequent placement at a different target position, which is then maintained at zero field (figs. S10 and S11) (*23*).

Electrically controlled movement of cargo

To show controlled movement of a cargo molecule attached to the arm, we used the three-color FRET system already employed in the stochastic switching experiments (Fig. 5A). In contrast to those experiments, the donor fluorophore is actively transported between two 9-nucleotide-long docking positions by rotating the arm with the help of the high torque extension at rotation frequencies of f = 1, 2, and 4 Hz, respectively. We observed alternating FRET traces (Fig. 5B) with the periodicity of the externally applied field. In agreement with the latching experiments (Fig. 4B), higher rotation frequencies correspond with an increase in the number of skips.

To demonstrate transport of inorganic nanoparticles by the robot arm, we attached a gold nanorod (AuNR) to one side of the 6HB arm and probed its plasmonic interaction with red and green fluorophores immobilized on the platform (Fig. 5C). As shown in Fig. 5D and fig. S12 (*23*), the AuNR alternately modulates the fluorescence of the fluorophores during rotation of the arm at the externally prescribed frequency. Electrical manipulation enables faster operation of switchable biohybrid plasmonic systems than previously achieved with the fuel-strand technique (*34*). More sophisticated systems involving multiple particles for the creation of switchable field enhancement or circular dichroism appear feasible (*35*).

Discussion

We have introduced electrical actuation as a viable strategy for fast, computer-controlled operation of biohybrid nanorobotic systems, which can exert forces at the molecular scale. Compared with nanoscale manipulation methods such as scanning probe techniques and optical or magnetic tweezers, electrical control is contact-free and can be implemented with low-cost instrumentation. The robotic movements achieved are at least five orders of magnitude faster than previously reported for the fastest DNA motor systems and are comparable to adenosine triphosphatase–driven biohybrids (*5*). The robot-arm system may be scaled up and integrated into larger hybrid

systems by a combination of lithographic and self-assembly techniques. For instance, the platforms can be easily connected to form long filaments with multiple DNA robot arms (fig. S13) (*23*) or to create extended lattices. The use of algorithmic self-assembly (*36*) will enable the creation of structures with different types of robot platforms with dedicated tasks. Lithographic patterning of the substrate (*37–39*) will further allow the fabrication of robot-arm arrays with defined platform orientations. By using nanostructured control electrodes, single robot arms could even be addressed individually, and their positioning state could act as a molecular mechanical memory. Combined with appropriate pickup and release mechanisms (*3, 40*), it is conceivable that this technology can also be applied to DNA-templated synthesis (*41*). Electrically clocked synthesis of molecules with a large number of robot arms in parallel could then be the first step toward the realization of a genuine nanorobotic production factory.

REFERENCES AND NOTES

1. J. D. Badjic, V. Balzani, A. Credi, S. Silvi, J. F. Stoddart, *Science* **303**, 1845–1849 (2004).
2. T. Kudernac *et al.*, *Nature* **479**, 208–211 (2011).
3. S. Kassem, A. T. L. Lee, D. A. Leigh, A. Markevicius, J. Solà, *Nat. Chem.* **8**, 138–143 (2016).
4. B. Lewandowski *et al.*, *Science* **339**, 189–193 (2013).
5. R. K. Soong *et al.*, *Science* **290**, 1555–1558 (2000).
6. P. W. Rothemund, *Nature* **440**, 297–302 (2006).
7. S. M. Douglas *et al.*, *Nature* **459**, 414–418 (2009).
8. J. S. Shin, N. A. Pierce, *J. Am. Chem. Soc.* **126**, 10834–10835 (2004).
9. S. J. Green, J. Bath, A. J. Turberfield, *Phys. Rev. Lett.* **101**, 238101 (2008).
10. T. Omabegho, R. Sha, N. C. Seeman, *Science* **324**, 67–71 (2009).
11. K. Lund *et al.*, *Nature* **465**, 206–210 (2010).
12. S. F. J. Wickham *et al.*, *Nat. Nanotechnol.* **6**, 166–169 (2011).
13. T. E. Tomov *et al.*, *ACS Nano* **11**, 4002–4008 (2017).
14. H. Gu, J. Chao, S.-J. Xiao, N. C. Seeman, *Nature* **465**, 202–205 (2010).
15. Z.-G. Wang, J. Elbaz, I. Willner, *Angew. Chem. Int. Ed.* **51**, 4322–4326 (2012).
16. E. Kopperger, T. Pirzer, F. C. Simmel, *Nano Lett.* **15**, 2693–2699 (2015).
17. Y. Yang *et al.*, *Chemistry* **23**, 3979–3985 (2017).
18. T. Tomaru, Y. Suzuki, I. Kawamata, S.-M. Nomura, S. Murata, *Chem. Commun.* **53**, 7716–7719 (2017).
19. A. E. Marras, L. Zhou, H.-J. Su, C. E. Castro, *Proc. Natl. Acad. Sci. U.S.A.* **112**, 713–718 (2015).
20. P. Ketterer, E. M. Willner, H. Dietz, *Sci. Adv.* **2**, e1501209 (2016).
21. B. Yurke, A. J. Turberfield, A. P. Mills Jr., F. C. Simmel, J. L. Neumann, *Nature* **406**, 605–608 (2000).
22. D. Y. Zhang, G. Seelig, *Nat. Chem.* **3**, 103–113 (2011).
23. See supplementary materials.
24. S. A. McKinney, C. Joo, T. Ha, *Biophys. J.* **91**, 1941–1951 (2006).
25. A. N. Kapanidis *et al.*, *Acc. Chem. Res.* **38**, 523–533 (2005).
26. D. J. Kauert, T. Kurth, T. Liedl, R. Seidel, *Nano Lett.* **11**, 5558–5563 (2011).
27. J. L. Viovy, *Rev. Mod. Phys.* **72**, 813–872 (2000).
28. Y. Klapper, N. Sinha, T. W. S. Ng, D. Lubrich, *Small* **6**, 44–47 (2010).
29. O. K. Dudko, G. Hummer, A. Szabo, *Proc. Natl. Acad. Sci. U.S.A.* **105**, 15755–15760 (2008).
30. F. Wei *et al.*, *Langmuir* **22**, 6280–6285 (2006).
31. B. Essevaz-Roulet, U. Bockelmann, F. Heslot, *Proc. Natl. Acad. Sci. U.S.A.* **94**, 11935–11940 (1997).
32. U. Bockelmann, P. Thomen, B. Essevaz-Roulet, V. Viasnoff, F. Heslot, *Biophys. J.* **82**, 1537–1553 (2002).
33. A. F. Sauer-Budge, J. A. Nyamwanda, D. K. Lubensky, D. Branton, *Phys. Rev. Lett.* **90**, 238101 (2003).
34. A. Kuzyk *et al.*, *Nat. Mater.* **13**, 862–866 (2014).
35. T. Zhang, N. Gao, S. Li, M. J. Lang, Q. H. Xu, *J. Phys. Chem. Lett.* **6**, 2043–2049 (2015).
36. R. D. Barish, R. Schulman, P. W. K. Rothemund, E. Winfree, *Proc. Natl. Acad. Sci. U.S.A.* **106**, 6054–6059 (2009).
37. A. Gopinath, P. W. K. Rothemund, *ACS Nano* **8**, 12030–12040 (2014).
38. A. Gopinath, E. Miyazono, A. Faraon, P. W. K. Rothemund, *Nature* **535**, 401–405 (2016).
39. M. B. Scheible, G. Pardatscher, A. Kuzyk, F. C. Simmel, *Nano Lett.* **14**, 1627–1633 (2014).
40. S. K. Kufer, E. M. Puchner, H. Gumpp, T. Liedl, H. E. Gaub, *Science* **319**, 594–596 (2008).
41. X. Li, D. R. Liu, *Angew. Chem. Int. Ed.* **43**, 4848–4870 (2004).

Science

A self-assembled nanoscale robotic arm controlled by electric fields

Enzo Kopperger, Jonathan List, Sushi Madhira, Florian Rothfischer, Don C. Lamb and Friedrich C. Simmel

ARTICLE TOOLS	http://science.sciencemag.org/content/359/6373/296
SUPPLEMENTARY MATERIALS	http://science.sciencemag.org/content/suppl/2018/01/18/359.6373.296.DC1
PERMISSIONS	http://www.sciencemag.org/help/reprints-and-permissions

Use of this article is subject to the Terms of Service